Topological surface states in ultrathin Bi 1 − x Sb x layers

Laëtitia Baringthon, Thi Huong Dang, Henri Jaffrès, Nicolas Reyren, Jean-Marie George, Martina Morassi, Gilles Patriarche, Aristide Lemaitre, François Bertran, Patrick Le Fèvre

Topological surface states in ultrathin $Bi_{1-x}Sb_x$ layers

Laëtitia Baringthon,[1,2,3] Thi Huong Dang,[1] Henri Jaffrès,[1] Nicolas Reyren,[1] Jean-Marie George,[1] Martina Morassi,[2] Gilles Patriarche,[2] Aristide Lemaitre,[2] François Bertran,[3] and Patrick Le Fèvre[3,*]

[1]*Unité Mixte de Physique, CNRS, Thales, Université Paris-Saclay, 91767 Palaiseau, France*

[2]*Université Paris-Saclay, CNRS, Centre de Nanosciences et de Nanotechnologies, 91120 Palaiseau, France*

[3]*Synchrotron SOLEIL, Boîte Postale 48, L'Orme des Merisiers, Saint-Aubin, 91192 Gif-sur-Yvette, France*

(Received 24 January 2022; revised 3 May 2022; accepted 27 May 2022; published 20 July 2022)

Topological insulator spin-polarized surface states are attractive for spintronic applications, in particular for spin-charge current interconversion, where extremely high conversion efficiencies are predicted. However, the contribution of topologically trivial bulk states is often disregarded although it may play a crucial role in the experimental results and extracted conversion efficiencies. The presence of bulk states at the Fermi level can be avoided by increasing the gap using the confinement effect appearing as the film thickness is reduced. We address this topic by growing $Bi_{1-x}Sb_x$ thin films (2.5–15 nm) by molecular beam epitaxy on InSb, BaF_2, and Si substrates. The surface electronic band structure is studied by angle-resolved photoemission spectroscopy. Two $Bi_{1-x}Sb_x$ surface states are observed in the gap for several Sb concentrations and thicknesses, across the topological insulator phase, scanning x between 7% and 30%. Tight-binding calculations of the surface states are in good agreement with the experiments, revealing their polarized nature. Surface states are still present at the Γ point for the thinnest films (2.5 nm), suggesting highly confined polarized states at the surface.

DOI: 10.1103/PhysRevMaterials.6.074204

I. INTRODUCTION

In the field of spin orbitronics, the discovery of quantum states at the surface of the three-dimensional (3D) topological insulators (TIs) [1] has unveiled new exciting opportunities. Indeed, their topologically protected conductive surface states are spin-momentum locked: The spin of the carriers is oriented perpendicular to their momentum. When a charge flows in the surface plane, this particular spin texture in momentum space generates a spin accumulation with the accumulated spin orientation locked by the current direction, usually transverse to it. This mechanism is called the Edelstein (or sometimes Rashba-Edelstein) effect (EE) [2]. In a reciprocal way, pure spin currents injected perpendicular to the conductive plane are converted into lateral charge currents via the inverse Edelstein effect (IEE [3]). For these TI surface states, spin-charge conversion efficiencies are found to be much larger than those in heavy metals originating from spin Hall effect (SHE), due to the fully polarized band structure of the surface states [4–7]. However, in most 3D TIs, the control of the Fermi level inside the gap is critical to limiting spurious parallel electron transport from the bulk bands. Moreover, most of the published experiments fail to provide clear evidence of the surface state contribution versus the bulk states to the conversion mechanisms, in particular to distinguish EE (or inverse EE) from SHE (or inverse SHE).

Despite being the first material predicted [6] and reported [8] as a 3D TI, $Bi_{1-x}Sb_x$ (BiSb) alloys have been neglected for spintronic applications for a long time because of their relatively small gap (about 30 meV) and complex band structure close to the Fermi level [9]. Investigations have mainly been focused on $Bi_2(Se_xTe_{1-x})_3$ compounds with larger band gap (up to 0.3 eV) and where nontrivial surface states are located around the Γ point in the reciprocal space [10]. More recently, it has been shown that BiSb might be a good candidate for spintronic and spin-orbit torque applications for magnetic random-access memories (SOTMRAM) [11,12], even though we are still lacking a clear understanding of the electronic states involved in the spin-to-charge current conversion.

The BiSb surface states have been investigated in single crystals [13] and thin films [14] using angle-resolved photoemission spectroscopy (ARPES), leading to a controversy about the number (three or two) of spin-polarized surface bands originating from the topological nature of BiSb. Close to the Γ point, there is a consensus about the existence of two spin-polarized surface states emerging from the bulk valence band continuum [13,15–17]. The controversial part is about the band structure close to the M point, where the theoretically predicted band inversion occurs for Sb concentration larger than 4% (throughout the paper, the atomic percentage is given) [18]. Nevertheless, the surface band topological nature is always associated to bulk band inversion and gap opening [11,13,8]. One way to increase the gap is to confine the electrons in very thin films, in order to increase the band splitting as is done in semiconductor quantum wells [19]. In epitaxial films, strain can have similar effects. Here, we report on the growth of BiSb thin films (from 2.5 to 15 nm with a focus on 15 nm films) for several Sb concentrations (7%, 15%, 21%, and 30%) on various substrates (InSb, BaF_2, and Si). The electronic surface properties are probed by ARPES as a function of the thickness and Sb concentration. We compare

*patrick.lefevre@synchrotron-soleil.fr

the electronic band structure revealed by ARPES with tight-binding (TB) calculations which predict the corresponding spin texture of the two surface states.

II. MBE GROWTH AND STRUCTURAL CHARACTERIZATIONS

We first study the BiSb growth by molecular beam epitaxy (MBE) on InSb, BaF_2, and Si substrates, all three with cubic crystalline structure. BiSb alloys have the same crystallographic structure as bulk Bi, namely, rhombohedral *A*7 structure with two atoms per unit cell. Here, we use the alternative hexagonal cell representation (described by a and c crystallographic parameters) where Bi (and its Sb alloys) appear as a stacking of hexagonal planes [20]. The hexagonal symmetry of the (111) cubic substrate planes is therefore suitable for epitaxial growth of BiSb (0001). Considering a $Bi_{0.79}Sb_{0.21}$ alloy with crystallographic parameters $a = 4.496$ Å and $c = 11.755$ Å at 298 ± 3 K [21], the resulting lattice mismatches are (along specific crystalline direction) −1.85% (InSb), 2.55% (BaF_2), and 17% (Si). Despite these mismatches, we demonstrate hereafter that BiSb growth remains epitaxial on these substrates at least up to a 15 nm thickness.

A critical part is the substrate surface preparation. For InSb, we repeat, twice, a cycle of Ar sputtering with 700 eV Ar ions (8×10^{-6} mbar pressure) during 20 min, followed by an annealing at 680 ± 10 K for 20 min. For BaF_2, we anneal the substrates at about 1150 K in vacuum (5×10^{-8} mbar residual pressure). Finally, the Si substrates were first cleaned in a HF:H_20 (40:60) solution during 30 s before introduction in vacuum and then were annealed at 1370 K in the MBE chamber (9×10^{-8} mbar residual pressure) for 15 min. This step is necessary to obtain a 7 × 7 surface reconstruction, observed by reflection high-energy electron diffraction (RHEED), prior to the BiSb deposition. We found that this surface reconstruction is required to obtain two-dimensional (2D) BiSb layers. RHEED patterns recorded with 25 keV electrons on each of these substrates before the BiSb growth are presented in the left side of Fig. 1(a).

BiSb is grown by codeposition from two Knudsen cells. Each cell flux is calibrated prior to the deposition using a quartz microbalance and the relative deposition rates are directly used to estimate the Sb concentration x. Typically, the Bi-growth rate is 0.1 Å /s. On InSb and BaF_2 substrates, we grow BiSb in a single step at room temperature (RT). The RHEED pattern remains streaky indicating a 2D epitaxial growth [see right part of of Fig. 1(a)]. For thick BiSb layers (above 5 nm), on a Si substrate, we use a two-step growth: the first 7 nm are grown at RT yielding a spotty RHEED pattern, typical for an island growth mode as discussed below. Then the film is annealed at around 500 K for about 10 min, until a 2D RHEED pattern is recovered. The remaining layer is grown at RT up to the targeted thickness (e.g., 15 nm), with a 2D growth mode according to RHEED measurements. Eventually, whatever the substrate, the films are postannealed at 500 K for about 10 min, in the growth chamber. The right side of Fig. 1(a) displays RHEED patterns at the end of a 15 nm thick BiSb deposition on the different substrates.

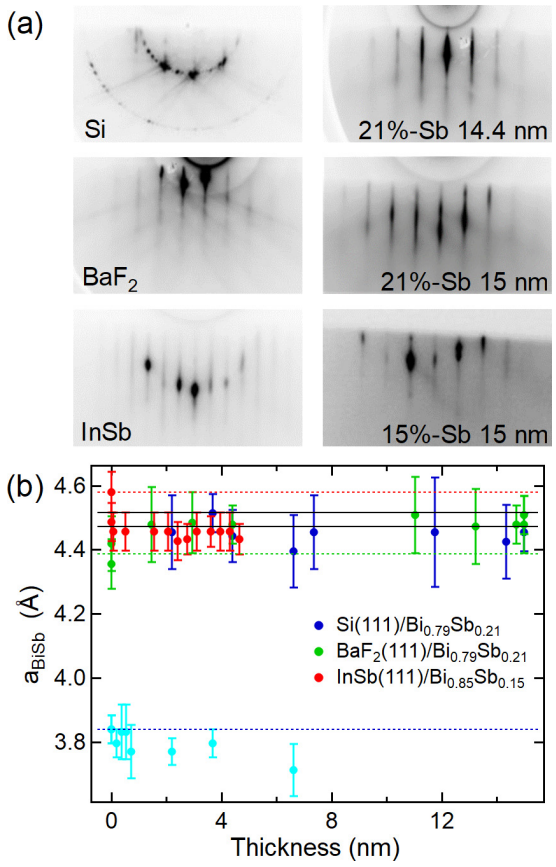

FIG. 1. RHEED analysis during growth. (a) RHEED patterns of the prepared substrates. Left column, from top to bottom: Si (111) (and its 7 × 7 reconstruction), BaF_2 (111), and InSb (1 1 1). Right column: RHEED patterns on 15 nm thick BiSb films, $Bi_{0.79}Sb_{0.21}$ for the first two, and $Bi_{0.85}Sb_{0.15}$ for InSb. (b) Evolution of the in-plane lattice parameter. Dashed lines (blue for Si, green for BaF_2, and red for InSb) indicate the substrate lattice parameters (used for calibration) and the solid black lines are the expected bulk parameter for $Bi_{0.79}Sb_{0.21}$ (lower one) and $Bi_{0.85}Sb_{0.15}$ (upper one). For the growth on Si, the RHEED pattern first reveals two families of diffraction lines attributed to the Si substrate (cyan) and the BiSb film (dark blue) (see text for details).

As demonstrated by the scanning transmission electron microscopy (STEM) cross sections, x-ray diffraction, and RHEED data, the BiSb epitaxial relationships on InSb, BaF_2, and Si substrates are mostly the following: BiSb (0001)⟨100⟩ direction parallel to the substrate (111)⟨211⟩ direction, and the substrate (111)⟨110⟩ is parallel to BiSb (0001)⟨110⟩. For BiSb grown on a Si substrate, the film is not fully single domain and STEM measurements reveal grains with 30° rotation of the crystal lattice, with the BiSb ⟨100⟩ direction oriented either along the ⟨110⟩ or the ⟨11$\bar{2}$⟩ directions of the Si substrate. This is further confirmed by atomic force microscopy measurements (not shown) displaying terraces with two families of orientations, 30° apart, only for samples grown on Si.

RHEED patterns are used to follow the in-plane film parameter during the BiSb growth [22] [see Fig. 1(b)]. The distances between two RHEED peaks are calibrated using the substrate lattice constant [dashed line in Fig. 1(b)].

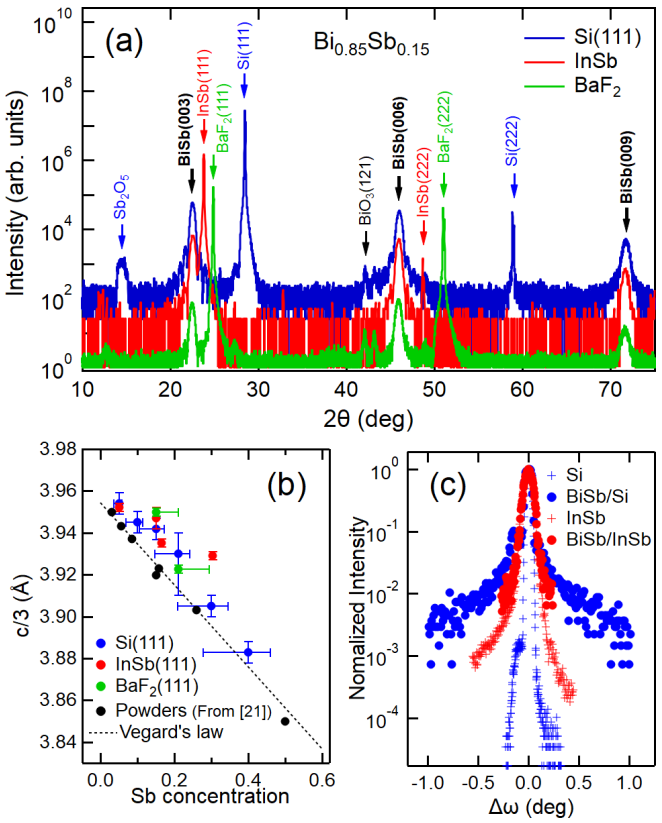

FIG. 2. *Ex situ* x-ray diffraction using Cu $K\alpha$ radiation on our BiSb samples. (a) θ-2θ diffractogram of a 15 nm thick BiSb film oxidized in air on Si (111) (blue curve), InSb (111) (red curve), and BaF_2 (111) (green curve). (b) Out-of-plane lattice parameter as a function of the Sb concentration extracted from XRD data. The dashed line corresponds to the out-of-plane lattice parameter expected from Vegard's law; the black points are reported powder measurements (extracted from [22]). Blue, red, and green points are measurements on our BiSb films on Si, BaF_2, and InSb, respectively. (c) Rocking curves measured on Si/BiSb (blue points) and InSb/BiSb (red points) superimposed on the substrates' rocking curves (blue and red crosses; the width is experimentally limited).

Independently of the substrate, the BiSb in-plane parameter very quickly (thickness < 1 nm) converges to values close to the BiSb bulk parameter [solid black line in Fig. 1(b)], i.e., about 0.450 nm, indicating a fast plastic relaxation (see below). During the two-step growth on Si, the RHEED pattern first reveals two families of diffraction spots, represented by two shades of blue in Fig. 1(b), attributed to the Si (cyan) substrate and the BiSb film (dark blue). This suggests that growth initially proceeds by island formation, with part of the Si substrate still diffracting electrons. The intermediate annealing promotes a 2D reconstruction and allows a subsequent 2D growth mode.

Further structural information about the films is obtained using x-ray diffraction (XRD) performed *ex situ*. XRD confirms long-range epitaxial growth of BiSb with its (0001) planes parallel to the (111) substrate plane, for all substrates. The film thickness is determined by fitting the finite size fringes, which confirms the targeted thickness within about 3%. The out-of-plane lattice parameter is determined by the

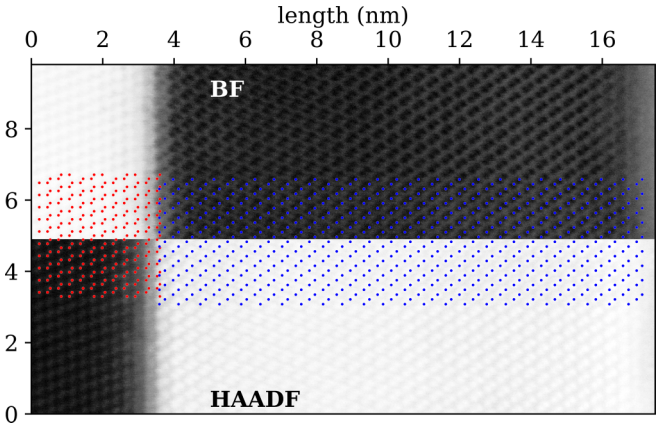

FIG. 3. HAADF (high-angle annular dark-field) and BF (bright-field) STEM measurements taken along the $[1\bar{1}0]$ direction of the Si(111)/$Bi_{0.79}Sb_{0.21}$ (15 nm) with overlaid calculated Si and BiSb atomic positions in red and blue, respectively.

XRD peak position. In Fig. 2(b), we report its dependence on Sb concentration, which follows the trend of Vegard's law observed for bulk powder samples [21] with a systematic shift of about $+2$ pm in c, or $+8\%$ in Sb concentration x. This deviation from Vegard's law cannot be explained straightforwardly by the strain imposed by the substrate, as the InSb and BaF_2 substrates produce opposite strains. The BiSb rocking curves [Fig. 2(c)] also reveal the dislocations in the film, which are observed as a broad linear part in the semilog plot around the Bragg peak position, when grown on Si. They probably originate from the two possible grain orientations of the islands during the first part of the growth.

To complete our structural characterization studies, we perform real-space imaging using aberration corrected scanning transmission electron microscopy (STEM) coupled with chemical analysis using energy-dispersive x-ray spectroscopy (EDX). Thin slabs of Si/BiSb and BaF_2/BiSb samples were prepared along the $[1\bar{1}0]$ and [112] substrate directions. The a- and c-axis parameters are extracted from the STEM pictures at higher magnification (field of views from 2 to 50 nm) and are both consistent with those extracted from RHEED measurement ($a = 0.45 \pm 0.02$ nm on BaF_2 and $a = 0.44 \pm 0.02$ nm on Si) and XRD ($c = 0.39 \pm 0.02$ nm on BaF_2 and $c = 0.40 \pm 0.02$ nm on Si). EDX along the growth direction reveals a Sb concentration gradient: For a 21% Sb nominal concentration, a variation from 15% to 24% is measured from the center layer to the top one, with a mean value of 21%. The origin of this gradient is probably related to the Bi surfactant effect. Similar results were obtained on BaF_2. To understand how the BiSb thin film accommodates the extremely large mismatch with the Si(111) substrate, we investigated this interface using high-magnification STEM (Fig. 3) both in bright field (BF) and in high-angle annular dark field (HAADF). The projections of BiSb and Si crystalline structures, using the bulk lattice parameters, are laid over the STEM micrograph. It evidences a commensurate interface between BiSb and Si (111) oriented layers, where six Bi or Sb atoms coincide with seven atoms along the $[1\bar{1}0]$ direction of the Si(111) substrate.

In summary, BiSb epitaxial growth is possible over a large range of substrates. Despite large mismatch and strain

relaxation over a few lattice parameters at most, the BiSb film orientation is identical to the substrate one. This rapid relaxation, even for small lattice mismatch (InSb) indicates that the interaction with the substrate is weak, close to a van der Waals coupling [23]. The deviation from Vegard's law as compared to bulk materials [Fig. 2(c)], however, remains unexplained as we can exclude Sb concentration shift (from the EDX), and as both STEM and XRD confirm an ordered BiSb crystalline structure (and not a solid solution).

III. ARPES MEASUREMENTS AND TIGHT-BINDING COMPUTATIONS

The influence of the thickness and Sb concentration on the BiSb surface states is probed by ARPES measurements, performed on the CASSIOPEE beamline at SOLEIL synchrotron. ARPES is a unique technique to probe the electronic band structure of solids. Synchrotron radiation gives access to state energy dispersion along k_z (i.e., perpendicular to the surface) using variable incident photon energy measurements. The lack of dispersion along z demonstrates the 2D nature of an electronic state. The first experimental evidences of the existence of such states were indeed brought about by ARPES experiments on BiSb alloys [13] and Bi_2Se_3 [7].

The BiSb thin films described above were grown in the MBE chamber connected to the ARPES experiment, allowing us to keep the surface in ultrahigh vacuum from the growth chamber to the analysis one. The films grown on BaF_2 could not be measured by ARPES due to the very large substrate band gap and the resulting charge accumulation, preventing ARPES measurements. Therefore, the ARPES measurements were only performed on films grown on Si(111) and InSb(111) substrates. The reciprocal space is calculated starting from the rhombohedral unit cell. It leads to a truncated octahedron 3D first Brillouin zone (BZ) presented in Fig. 4(a). The surface states can be studied in the 2D surface BZ which is obtained by projecting the 3D first BZ along the surface normal direction [14]. It gives the hexagonal surface first BZ presented in the top of Fig. 4(a). The main symmetry points are $\bar{\Gamma}$, $\bar{K}$ and $\bar{M}$, $\bar{M}$, being the projection of the L and X points of the 3D BZ on the (111) plane. In the following, the k_x direction was chosen to be along $\bar{\Gamma}\bar{M}$ and k_y along a perpendicular $\bar{\Gamma}\bar{K}$ direction. Theory predicts that BiSb alloys are topological insulators for Sb concentrations between 7% and 22% [24]. A topological surface state was also experimentally evidenced in this composition range both in cleaved crystals [13] and in a 120 nm thick film of BiSb [14]. We investigated by ARPES a series of BiSb alloys films with Sb concentrations from 7% to 30% and of thicknesses from 2.5 to 15 nm. In the ARPES experiment, the photon beam is coming at 45° from the electron analyzer whose entrance slit is vertical. The photoelectrons are therefore collected in a vertical plane (defined by the slit and the analyzer axis) in an emission angle range of around 30° (15° above and below the horizontal direction). The sample can be rotated around its surface normal to align any surface crystallographic axis parallel to the entrance slit of the electron analyzer. The band dispersion along this peculiar direction is then directly measured on the analyzer 2D detector. A rotation around a horizontal axis contained in the sample surface allows us

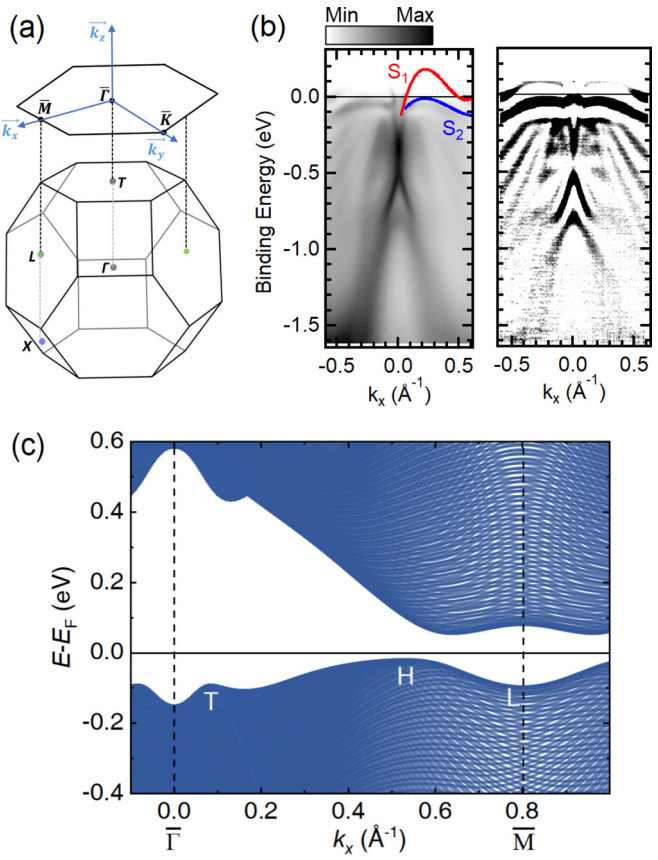

FIG. 4. (a) 3D first Brillouin zone of BiSb and its projected 2D Brillouin zone on the (111) surface. (b) ARPES intensity plot recorded on a 5 nm thick $Bi_{0.93}Sb_{0.07}$ film grown on Si(111) (left) and the corresponding second derivative (right) around the $\bar{\Gamma}$ point. k_x is along the $\bar{\Gamma}\bar{M}$ direction. Data are acquired using linear horizontal polarized light. The red and blue solid lines are guides to the eye, corresponding to the S_1 and S_2 surface states. (c) Calculated representation of the T, H, and L bands along the Γ-M direction obtained for $Bi_{0.79}Sb_{0.21}$ (in the $0.22 > x > 0.04$ semiconducting range). It has been obtained from the projection of the bulk states calculated by TB onto this direction (the surface states are absent). There is a band inversion at L and one can observe that the gap is nearly closed by the H band as predicted in Fig. 5 of Ref. [20].

to shift this dispersion on the detector while a last rotation, around the sample vertical axis, is used to scan the reciprocal space for a complete measurement of the band structure and Fermi surfaces. In all this work, the Fermi level for a data set was determined by angle-integrating (about 30°) the spectrum recorded at $\bar{\Gamma}$ and by fitting the obtained DOS with a Fermi function.

Figure 4(b) displays a typical band dispersion recorded on a 5 nm thick $Bi_{0.93}Sb_{0.07}$ film grown on Si(111) around the $\bar{\Gamma}$ point in the $\bar{\Gamma}\bar{M}$ direction, acquired at room temperature using linear horizontal polarization of the light. Both surface states, S_1 and S_2, are clearly visible. The S_1 state (red solid line) takes a conelike shape around $\bar{\Gamma}$. It is cut by the Fermi level but reappears on both edges of the image. S_2 (blue dotted line) has a flatter dispersion.

To get a better insight at these dispersions we have developed a tight-binding (TB) model [25] to describe the BiSb

electronic band structure. This approach is well suited for TI and gives a good description of the surface state spin texture in pretty close agreement with the one derived from density functional theory developed for pure Bi surfaces [26–28]. The rhombohedral $A7$ structure is described by two atoms per unit cell, forming then a bilayer (BL). From a TB computational point of view, BiSb slabs are obtained by stacking the BLs along the (111) direction (z axis) with two different plane-to-plane distances. We constructed our Hamiltonian on the basis of the work of Ref. [25] using the generalization of the sp^3 TB-model Hamiltonian proposed for bulk Bi and Sb crystals [9], adapted to BiSb alloys [6] and completed by the introduction of additional surface potential terms when dealing with thin layers (treatment in slabs) [25,29,30]. In particular, the hopping parameters for the BiSb alloys are obtained by using the virtual crystal approximation (VCA) according to [6]

$$V_C^{\mathrm{BiSb}} = xV_C^{\mathrm{Sb}} + (1-x^2)V_C^{\mathrm{Bi}},$$

where x is the antimony content; V_C^{Sb} and $\mathrm{V}_C^{\mathrm{Bi}}$ are the respective hopping parameters of Sb and Bi taken from Ref. [9].

We note $\hat{\sigma}_\alpha$, the spin index on each atom. The hopping terms among the atomic orbitals are decomposed into inter- and intra-BL hopping terms. The inter-BL off-diagonal hopping term $H_{21\text{-}1}$ between atoms (plane) 1 and atoms (plane) 2 consists of the nearest-neighbor (second index: 1) coupling in the bulk Bi Hamiltonian, whereas the intra-BL hopping term consists of two parts, H_{11} and $H_{12\text{-}2}$, which represent, respectively, the third and second nearest neighbor (second index: 2) terms.

We considered the overall TB Hamiltonian according to

$$\hat{H}_{\mathrm{TB}} = \hat{H}_0 + \hat{H}_{\mathrm{SO}} + \hat{H}_\gamma,$$

where $\hat{H}_0 = \sum_{i,j}^{\mu,\nu} |i\mu\rangle V_{i\mu}^{j\nu} \langle j\nu|$ represents the hopping Hamiltonian (i, j are the atoms; μ, ν are the orbitals), $\hat{H}_{\mathrm{SO}} = \frac{\hbar}{4m^2c^2}(\hat{\nabla}V \times \hat{p}).\hat{\sigma}$ the spin-orbit term and $\hat{H}_\gamma$ the Rashba surface potential induced by the deformation of the surface orbitals due to the local electric field. Indeed, due to the symmetry breaking at the surface, a Rashba spin-orbit interaction term must be taken into account in the Hamiltonian at the two surface planes. We model such effect for the sp^3 basis by using the approach of Ast and Gierz [29,30] for $\hat{H}_\gamma$ considering two additional surface hopping terms γ_{sp} and γ_{pp} acting, respectively, between the surface s-p_z and p_x-p_z (or p_y-p_z) orbitals. We thus add the Hamiltonian term $\hat{H}_\gamma$ of the following form:

$$\hat{H}_\gamma = \begin{cases} \pm\gamma_{pp}\cos(\theta)\ (i,j) \equiv (p_x, p_z) \\ \pm\gamma_{pp}\sin(\theta)\ (i,j) \equiv (p_y, p_z)\ , \\ \pm\gamma_{sp}\ (i,j) \equiv (s, p_z) \end{cases}$$

where the + (–) sign corresponds to the uppermost (lowermost) atomic plane and θ is the angle between the direction joining the two atoms considered and the x direction. We then restrained ourselves to the in-plane surface hopping as for a pure 2D system. The best agreement with ARPES results is found for $\gamma_{sp} = 0.3$ eV and $\gamma_{pp} = -0.4$ eV for $x = 0.07$ slightly departing from the values given for pure Bi, i.e., $\gamma_{sp} = 0.45$ eV and $\gamma_{pp} = -0.27$ eV [25], with opposite sign for the top and bottom surfaces due to the opposite direction of the potential gradient. We emphasize that these surface terms are required to correctly reproduce the surface state dispersion as observed by ARPES experiments. The size of the Hamiltonian $\hat{H}(k_x,\ k_y)$ to diagonalize is $16N \times 16N$ where N is the number of bilayers (BLs). Once the Green's function of the multilayer system is defined as

$$\hat{G}(E, k_x, k_y) = [E + i\delta - \hat{H}(k_x, k_y)]^{-1};$$

the partial density of states (DOS) $\rho(E)$ versus the energy E equals $\rho(n, E) = -\frac{1}{\pi}\mathrm{Im\ Tr}\hat{G}(E, k_x, k_y)$ whereas the spin density of states (spin DOS) with spin along the α direction is $s_\alpha(E) = \frac{1}{\pi}\mathrm{Tr\ Im}[\hat{\sigma}_\alpha\hat{G}(E, k_x, k_y)]$. δ is the typical energy broadening (10 meV) and the trace (Tr) is applied over the considered sp^3 orbitals on a given BL index (n). The energy zero ($E = 0$) refers to the Fermi level position.

Throughout the paper, our calculations are performed for relaxed BiSb alloys corresponding to a bulk lattice parameter following Vegard's law, as observed experimentally on Fig. 2(a) at least for layers with thickness larger than or equal to 5 nm. We now give more details about our findings on the band hierarchy and TI properties phase diagram and compare it to what is proposed by Lenoir and Caillat (Fig. 5 of Ref. [20]) concerning the evolution of the band gap, in particular when it is indirect. This latter case corresponds to a gap defined between the lower-energy state in the conduction band (CB) near the $\bar{M}$ point along the $\bar{\Gamma}$ $\bar{M}$ direction and the higher-energy state in the valence band (VB) as shown in Fig. 4(c). A large indirect band gap represents a strong requirement for the appearance of topological states at the BiSb surface.

First, we checked that the phase diagram of the $\mathrm{Bi_{1-x}Sb_x}$ electronic band structure obtained with the chosen parametrization well corresponds to the one given in Ref. [24] in the $x = $ [0-0.2] window before extending the calculation to the $x = $ [0.2-0.4] region. The main evolution of the band structure concerns the crossings between (i) the L_a and L_s bands related to the direct gap [8,18] and, (ii) the L_s and T bands as well as L_s and H related to the indirect gap. One observes thus that the indirect gap increases from $x = 0.07$ to $x = 0.15$ before decreasing from $x = 0.21$ up to $x = 0.36$ for which the latter closes as expected due to the rise of the middle H bands [12–18] [see Fig. 4(c)].

We extended this model, validated on bulk compounds, to deal with the quantization effects in BiSb slabs and we calculated the dependence of the direct gap at the $\bar{M}$ point versus the number N of bilayers. Our calculations predict [Fig. 5(a)] that the direct gap increases on reducing the BiSb layer thickness from 100 BLs down to 6 BLs for $x = 0.07$, 0.15, 0.21, 0.3, and 0.4, to reach almost 1 eV for $x = 0.3$ and $x = 0.4$ in a six-BL (2.5 nm) film. The case of pure Bi ($x = 0$) shows the same trends of a gap increase on decreasing the thickness (see, e.g., Ref. [32]), without, however, displaying any band inversion (the L_s band lies above the L_a band) [20]. Refined analysis shows that such a gap increase in BiSb alloys is due, in parallel, to a rise in energy of the conduction band and a lowering of the valence bands as expected for both electron and hole pictures of a semiconductor quantum well confined along the growth axis. The increase is much more pronounced at the $\bar{M}$ point than near $\bar{\Gamma}$ owing to the large

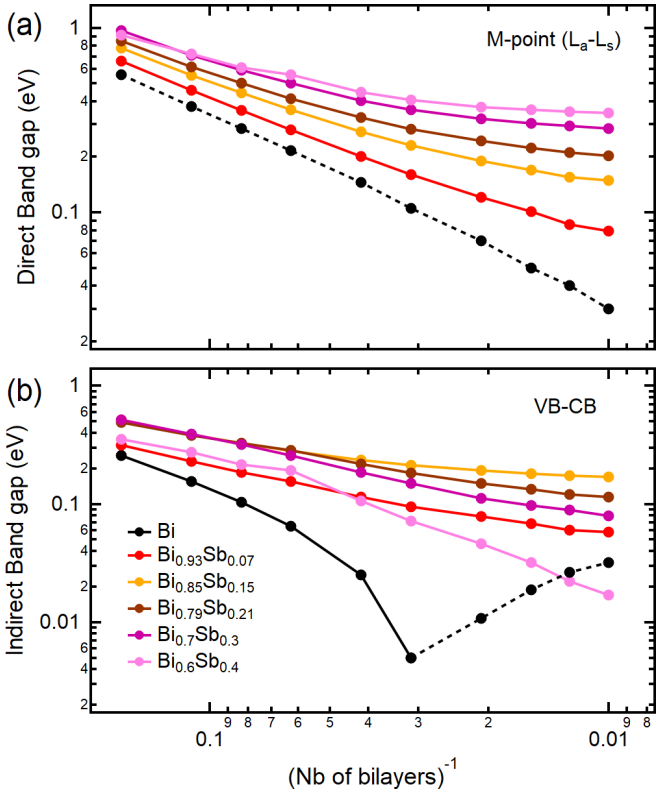

FIG. 5. Quantization effects on the band gaps of $Bi_{1-x}Sb_x$. (a) Direct energy gap at the $\bar{M}$ point calculated by TB for different $Bi_{1-x}Sb_x$ layers as a function of the inverse of number of bilayers (BLs). A positive gap means that the L_a bands sets above the L_s bands (band inversion). Pure Bi presents no band inversion (dash line). (b) Indirect band gap (energy difference between the bottom of the CB and top of the valence band along the $\bar{\Gamma}\bar{M}$ line point calculated by TB techniques for different $Bi_{1-x}Sb_x$ layers vs the inverse of number of bilayers (BLs). A positive band gap (solid line) means a semiconductor property whereas a negative band gap for pure Bi should be associated to a semimetal property (dash line). The quantization effects leads to a crossover for Bi from semimetal (thick layer) to semiconductor for a critical thickness of about 15 nm (36 BLs).

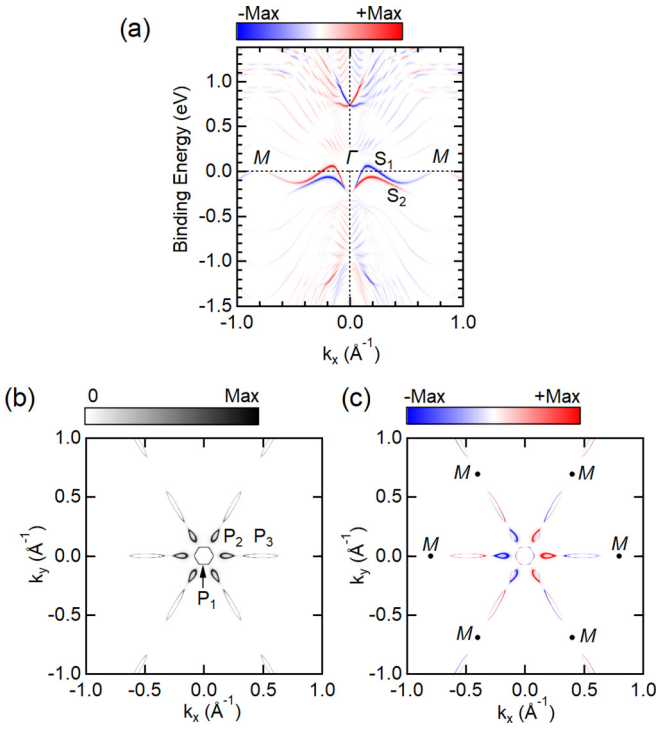

FIG. 6. Tight binding calculation of the band structure of a 12 BL (∼5 nm) film of $Bi_{0.93}Sb_{0.07}$. (a) Electronic band structure along the $\bar{\Gamma}\bar{M}$ direction showing the bulk dispersions and the two surface states spin-resolved DOS σ_y. (b) Plot of the total density of state (DOS) of the first surface plane of $Bi_{0.93}Sb_{0.07}$ projected onto the 2D BZ showing the three different electron (S_1, S_3) and hole pockets (S_2). (c) Calculated in-plane component of the spin-resolved DOS σ_y of the first surface plane of $Bi_{0.93}Sb_{0.07}$ along k_x. The blue (respectively, red) color represents a positive (negative) projection of the spin.

extension of the surface states around $\bar{M}$ as found in the case of pure Bi [26].

Our TB calculations also display a large increase of the indirect gap on decreasing $Bi_{1-x}Sb_x$ layer thickness for $x = 0.07$, 0.15, 0.21, 0.3, and 0.4 [Fig. 5(b)], thus being more and more favorable to the presence of a topological state at surfaces (S_1). The $x = 0.4$ corresponds to the gap closure in the bulk, occurring for large N (for $N > 100$, the gap is smaller than 20 meV). However, in this case, when $N < 12$ (thickness of about 5 nm), the slope in the curve giving the gap vs N changes due to the anticrossing between the two surface states. This corresponds to a H point at the same level or higher compared to the minimum L_a band along the $\bar{\Gamma}\bar{M}$ line [12]. By comparison, the transition is found at $x = 0.36$ close to $x = 0.3$ in Ref. [12] and $x = 0.22$ in Ref. [1]. These predictions could, however, not be confirmed by our photoemission experiments. First, as we only probe the occupied states, we would only measure the position of the valence band maximum with respect to the Fermi level and not the whole band gap. Second, as already observed in previous studies [14], even the occupied T, H, and L bulk bands are hardly visible in the spectra.

We now turn to the description of the morphology and spin texture of the two surface states (S_1 and S_2) for $x = 0.07$. The electronic band structure of $Bi_{0.93}Sb_{0.07}$ was calculated for 12 BLs ($\simeq$ 5 nm). Its band dispersion along $\bar{\Gamma}\bar{M}$ ($k_x = -0.8, 0.8$ Å^{-1}) is plotted in Fig. 6(a), in excellent agreement with the ARPES data [Fig. 4(b)]. Figure 6(a) also shows the spin-resolved DOS of both the bulklike band structure and the surface states S_1 and S_2 in the bulk band gap. S_1 and S_2 are two fold degenerate because of the two identical top and bottom surfaces in the present calculations. The color code in Fig. 6(a) represents the spin DOS oriented along y for the top surface atomic plane, ρ_{σ_y} ($n = 1$). A positive (respectively, negative) spin DOS for positive (negative) k_x around $\bar{\Gamma}$ is observed. Note that the sign of this Rashba field is opposite around the $\bar{M}$ point (close to 0.8 Å^{-1}). The momentum-resolved density of states (DOS) within the 2D Brillouin zone, $\rho(n = 1, E = 0\,\text{eV}, k_x, k_y)$ is displayed in Fig. 6(b) for the surface bilayer ($n = 1$) calculated at the Fermi level ($E_F = +0$ eV), i.e., the Fermi surface. In agreement with the ARPES data, E_F only intercepts the S_1 and S_2 surface states. The Fermi surface firstly reveals the sixfold

symmetry related to the rhombohedral $A7$ structure, with the hexagonal-like electron pocket appearing around the $\bar{\Gamma}$ point, designated by $P1$ in Fig. 6(b). On adding the surface hopping term, six hole lobes and six extra electron lobes labeled $P2$ and $P3$ appear [Fig. 6(b)]. $P2$ is very sensitive to the Fermi level position and may disappear when the surface hopping terms are not properly included, as noticed in the case of pure Bi [25]. Moreover, the typical electron pocket $P1$ structure can be generally found in the 0%–40% Sb concentration range when the Rashba surface hopping is properly taken into account.

The spin-resolved DOS $[\rho_{\sigma_y}(n = 1, E = 0\ \text{eV}, k_x, k_y)]$ at the Fermi energy ($E_F = 0$) and projected onto the top $Bi_{0.93}Sb_{0.07}$ surface BL plane are shown in Fig. 6(c), giving the in-plane σ_y spin component for $S_{1,2}$. The plot highlights the symmetry of the corresponding spin splitting near the $\bar{\Gamma}$ point ($P1$ pocket; red represents a positive projection of the σ_y spin component whereas blue represents a negative projection) indicating a helical spin texture resulting from an effective Rashba field. Indeed, near $\bar{\Gamma}$ along the $\bar{\Gamma}\bar{M}$ direction (k_x), the spin is mainly oriented along $\pm\hat{y}$ (for the k_y direction it is mainly along $\pm\hat{x}$, not shown). The S_1 spin texture is then observed to be rather similar to what is expected from a pure 2×2 Rashba model except for the reminiscence of the hexagonal symmetry away from the $\bar{\Gamma}$ point as evidenced in experiments on Bi(111) crystals [31]. In more details, for $P1$ (S_1 band), $\hat{\sigma}$ lies mainly along the pocket structure. For the $P2$ hole pocket (S_2 band), the direction of $\hat{\sigma}$ is opposite to that of the nearby $P1$ pockets. For the $P2$ and $P3$ pockets, the polarization is almost constant (roughly perpendicular to k) and opposite between the two surface bands. These numerical observations are also consistent with previous conclusions raised for pure Bi [32], on which σ is not always exactly perpendicular to the wave vector k for S_2. This originates from the nonparabolic band structure, indicating that the spin structure cannot be fully described by a simple Rashba model. More complex terms generally arise in the Hamiltonian due to the specific (111) texture characterized by an elongated hexagon along $\bar{\Gamma}\bar{M}$. This shows that TB modeling becomes essential to correctly describe the full Brillouin zone. The bottom surface, not relevant in our case, displays opposite spin texture as expected from simple symmetry arguments.

Moreover, concerning the "bulk" properties and in relationship with our previous discussion of quantization effects, one can observe that the band structure is composed of a series of confined states separated in energy and their energy splitting increases on reducing the layer thickness. It is particularly clear in the ARPES data where three quantized bands in the valence band close to the $\bar{\Gamma}$ point are clearly observed [Fig. 4(b)]. The morphology of these bands is perfectly reproduced by our TB slab calculations and their properties are largely discussed in the case of pure Bi in Ref. [28].

An experimental Fermi surface is shown in Fig. 7(a) for a $Bi_{0.85}Sb_{0.15}$ 15 nm thick film grown on Si (111). It is obtained by measuring the band dispersion along $\bar{\Gamma}\bar{K}$. As predicted by the TB calculations, the Fermi surface has a sixfold symmetry, with a hexagonal core centered at $\bar{\Gamma}$, surrounded by petals pointing along the $\bar{\Gamma}\bar{M}$ directions. The hexagonal core ($P1$) is associated to the S_1 state, while the first petals, hole pockets ($P2$), are associated to the S_2 state. Going further

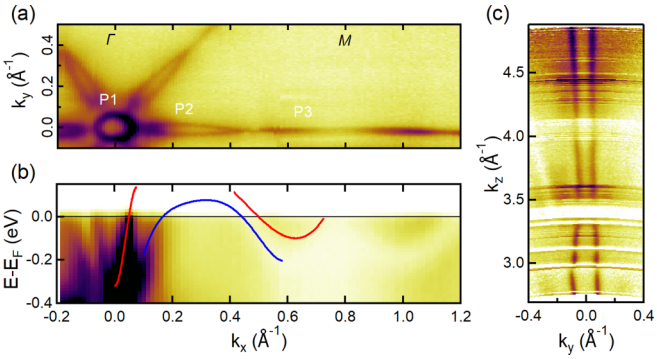

FIG. 7. ARPES recorded on Si(111)/$Bi_{0.85}Sb_{0.15}$(15 nm) measured at room temperature with linearly vertical polarized light at 25.2 eV. (a) Fermi surface produced by averaging the intensity in a 5 meV energy range around the Fermi level. (b) Cross section along $\bar{\Gamma}\bar{M}$ direction. (c) Fermi surface in the k_y-k_z plane, showing the nondispersive nature of the S_1 surface states.

toward the $\bar{M}$ point, another petal is formed by the S_1 band, which again crosses the Fermi level, and thus forms an extra electron pocket ($P3$). This is schematized in Fig. 7(b) which shows the energy dispersion along the $\bar{\Gamma}\bar{M}$ direction. Assuming that there is no electronic spin degeneracy due to the TI spin-momentum locking property, the carrier density can be estimated from the areas of the pockets at the Fermi level. It is about 3×10^{13} electrons/cm^2 for S_1 and 1×10^{14} holes/cm^2 for S_2. Note that the bulk states are not directly observed in these ARPES measurements. Therefore, we have no direct evidence of band inversion and bulk gap in our samples. However, the nontrivial phase of a topological insulator can also be characterized by the number of crossings of the Fermi level by the surface states between two time-reversal invariant momenta, $\bar{\Gamma}$ and $\bar{M}$, of the first Brillouin zone. An insulator is classified as nontrivial if at least one surface state presents an odd number of crossings, meaning it remains gapless whatever the Fermi level position is. In the present case, the second petal stops close to $\bar{M}$, showing that there is here an additional crossing of the Fermi level by S_1. Hence, the shape of the Fermi surface, especially in the vicinity of the $\bar{M}$ point, is a convenient indicator of the S_1 topological nature. Last, the 2D nature of these surface states is demonstrated in Fig. 7(c), where the Fermi surface in the (k_y-k_z) plane is obtained by varying the photon energy. The intersections of the two S_1 branches with the Fermi level are clearly visible as two (nearly) straight lines, showing that this state does not disperse perpendicular to the surface.

The detailed evolution of the Fermi surface and the $\bar{\Gamma}\bar{M}$ dispersion with Sb concentration (from 7% to 30%) for 5 nm thick films is illustrated in Fig. 8 (left column). The $\bar{M}$ point position with respect to the $\bar{\Gamma}$ point remains the same within the k resolution, since the in-plane lattice parameter only varies by 0.01% in this concentration range. The $P1$-hexagonal electron pocket at $\bar{\Gamma}$ does not change significantly in size but a noticeable expansion of $P2$ is observed with increasing x. This is also visible in the dispersions along the $\bar{\Gamma}\bar{M}$ direction (right column of Fig. 8). Another obvious change is the shape of the $P3$ petal. It appears to be open at $\bar{M}$ for the 7% compound, indicating an even number of crossings

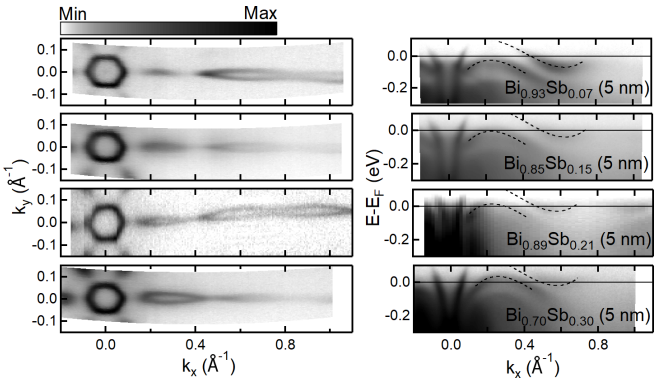

FIG. 8. ARPES dependence on Sb concentration: Left column: Fermi surfaces recorded on BiSb alloys with 7%, 15%, 21%, and 30% of Sb (from top to bottom) in 5 nm films. Right column: Cross sections of the same data sets showing the band dispersion along the $\bar{\Gamma}\bar{M}$ direction. The dotted lines are guides for the eye.

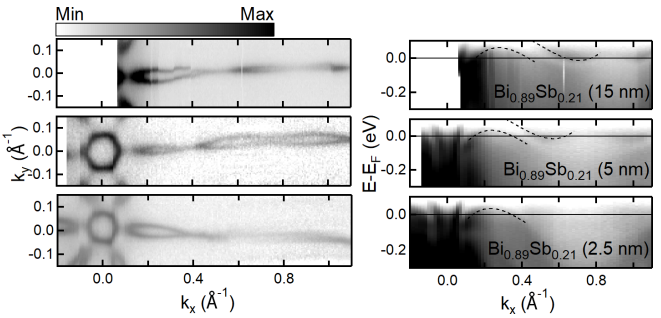

FIG. 9. ARPES dependence on film thickness: Left column: Fermi surfaces recorded on BiSb alloys with 21% of Sb in 15, 5, and 2.5 nm films. Right column: Cross sections of the same data sets showing the band dispersion along the $\bar{\Gamma}\bar{M}$ direction. The dotted lines are guides for the eye.

for this state with the Fermi level. In the $\bar{\Gamma}\bar{M}$ dispersion, S_1 indeed stays below the Fermi level around $\bar{M}$. As the Sb concentration increases, S_1 moves up in energy (relative to the Fermi level). In the 15%–21% Sb concentration range, it seems to reach the Fermi level for an additional crossing close to $\bar{M}$ and $P3$ closes. At a concentration of 30 % of Sb, S_1 is above E_F. The shift of S_1 from below to above the Fermi level close to the $\bar{M}$ point as a function of the concentration has been attributed to the L band inversion at the $\bar{M}$ point when increasing the Sb concentration [14]. Except for $P1$ around $\bar{\Gamma}$, the behavior of the petals mimics a downward shift of the Fermi level in a rigid (surface) band structure, as observed from first-principles calculations [32]. The evolution of the surface band structure with Sb concentration is very well described by Benia *et al.* for thick (120 nm) BiSb films [14]. For Sb concentration below 3%, they show that two adjacent $P3$ petals are connected at the $\bar{M}$ point. A gap between these two adjacent $P3$ petals opens at $\bar{M}$ for Sb concentration between 7% and 60%), before $P3$ disappears in pure Sb. What we see here in the 7%–30% Sb concentration range is a more pronounced evolution of the S_1 state around $\bar{M}$, with a shift upward in energy resulting in a S_1 state above the Fermi level around 30 at. % Sb (not observed by Benia *et al.*). We believe that this is due to the much smaller thicknesses of our films (5 nm). Our tight-binding calculations give a very large evanescence length (of the order of 10 nm) of the S_1 surface state at $\bar{M}$. A coupling of the two 2D states from the two opposite surfaces of the BiSb film is then possible, at least in this $\bar{M}$ region of the reciprocal space (evanescence lengths at $\bar{\Gamma}$ are much smaller and of the order of 5 Å). Such coupling has also been experimentally observed by transport measurements in Bi_2Se_3 thin films [33]. Our study therefore also highlights these confinement effects in the surface band structure.

The evolution for a 21% Sb compound for thicknesses from 2.5 to 15 nm is displayed in Fig. 9. The 15 nm thick film presents a well-defined $P3$ petal ending at $\bar{M}$ but when the thickness decreases, this petal opens at $\bar{M}$, as the S_1 surface state energy seems to shift downward below the Fermi level. The petal also becomes more and more blurry in this region. By reducing the thickness, effects due to confinement perpendicular to the surface also appear in the spectra, as can be seen in Fig. 4(b). A family of bands (three or four) can be seen below S_2 on the second derivative image, converging at $\bar{\Gamma}$ at roughly −0.2 eV binding energy, very similar to the quantum well states observed in pure Bi films [34]. Another possible explanation is the effect of the interference on the surface local DOS of the two opposite surface states near the $\bar{M}$ point at small thickness [35].

IV. CONCLUSION

In conclusion, we demonstrate epitaxial growth of thin BiSb layers on diverse substrates, including Si. The ARPES study clearly evidences two surface states, S_1 and S_2, as already observed in thicker BiSb samples. As a function of thickness and concentration, we observe slight modifications of the surface states near the Γ point. In most of the cases, by counting the Fermi level crossing by S_1, we conclude that this surface state is topologically nontrivial. There are two situations where the topological nature of S_1 is not clear; first, for small concentration (7%), where the band stays below the Fermi level near the $\bar{M}$ point, and second, for the thinner layer (2.5 nm, 21% Sb) and the larger concentration (5 nm, Sb 30%) when the electron pocket ARPES signal near $\bar{M}$ vanishes. Importantly, in none of our measurements could we observe any bulk states at the Fermi level, which indicates that the BiSb thin films are indeed good candidates to probe Edelstein or inverse Edelstein effects. Nevertheless, particular attention needs to be paid to the band bending effect as well as chemical reactivity at the interface when capping BiSb for *ex situ* measurements [36,37]. Finally, the TB calculations performed on this system demonstrate the specific Rashba-like spin texture of the surface states. The remarkable agreement of ARPES experimental data with TB calculations suggests a nearly fully polarized spin texture in BiSb, which is the most desirable case for spin-charge conversion processes and their related spintronic applications.

ACKNOWLEDGMENTS

This work is supported by a public grant overseen by the French National Research Agency (ANR) as part of

the "Investissements d'Avenir" program (Labex NanoSaclay, Reference No. ANR-10-LABX-0035), TOP-RISE Project No. ANR-16-CE24-0017, and by the French RENATECH network.

[1] M. Z. Hasan and C. L. Kane, Colloquium: Topological insulators, Rev. Mod. Phys. **82**, 3045 (2010).

[2] V. M. Edelstein, Spin polarization of conduction electrons induced by electric current in two-dimensional asymmetric electron systems, Solid State Commun. **73**, 233 (1990).

[3] J. C. Rojas-Sanchez, L. Vila, G. Desfonds, S. Gambarelli, J. Attanè, J. De Teresa, C. Magén, and A. Fert, Spin-to-charge conversion using Rashba coupling at the interface between nonmagneticmaterials, Nat. Commun. **4**, 2944 (2013).

[4] S. Zhang and A. Fert, Conversion between spin and charge currents with topological insulators, Phys. Rev. B **94**, 184423 (2016).

[5] J.-C. Rojas-Sánchez, S. Oyarzún, Y. Fu, A. Marty, C. Vergnaud, S. Gambarelli, L. Vila, M. Jamet, Y. Ohtsubo, A. Taleb-Ibrahimi, P. Le Fèvre, F. Bertran, N. Reyren, J.-M. George, and A. Fert, Spin to Charge Conversion at Room Temperature by Spin Pumping into a New Type of Topological Insulator: α-Sn Films, Phys. Rev. Lett. **116**, 096602 (2016).

[6] J. C. Teo, L. Fu, and C. Kane, Surface states and topological invariants in three-dimensional topological insulators: Application to $Bi_{1-x}Sb_x$, Phys. Rev. B **78**, 045426 (2008).

[7] D. Hsieh, Y. Xia, D. Qian, L. Wray, J. Dil, F. Meier, J. Osterwalder, L. Patthey, J. Checkelsky, and N. P. Ong, A tunable topological insulator in the spin helical Dirac transport regime, Nature (London) **460**, 1101 (2009).

[8] D. Hsieh, Y. Xia, L. Wray, D. Qian, A. Pal, F. Meier, J. Osterwalder, G. Bihlmayer, C. Kane, and Y. Hor, Observation of unconventional quantum spin textures in topological insulators, Science **323**, 919 (2009).

[9] Y. Liu and R. E. Allen, Electronic structure of the semimetals Bi and Sb, Phys. Rev. B **52**, 1566 (1995).

[10] L. Bao, L. He, N. Meyer, X. Kou, P. Zhang, Z.-g. Chen, A. V. Fedorov, J. Zou, T. M. Riedemann, and T. A. Lograsso, Weak anti-localization and quantum oscillations of surface states in topological insulator Bi_2Se_2Te, Sci. Rep. **2**, 1 (2012).

[11] N. H. D. Khang, Y. Ueda, and P. N. Hai, A conductive topological insulator with large spin Hall effect for ultralow power spin–orbit torque switching, Nat. Mater. **17**, 808 (2018).

[12] Z. Chi, Y.-C. Lau, X. Xu, T. Ohkubo, K. Hono, and M. Hayashi, The spin Hall effect of Bi-Sb alloys driven by thermally excited Dirac-like electrons, Sci. Adv. **6**, 2324 (2020).

[13] D. Hsieh, D. Qian, L. Wray, Y. Xia, Y. S. Hor, R. J. Cava, and M. Z. Hasan, A topological Dirac insulator in a quantum spin Hall phase, Nature (London) **452**, 970 (2008).

[14] H. M. Benia, C. Strasser, K. Kern, and C. R. Ast, Surface band structure of $Bi_{1-x}Sb_x$ (111), Phys. Rev. B **91**, 161406(R) (2015).

[15] C. R. Ast and H. Höchst, Electronic structure of a bismuth bilayer, Phys. Rev. B **67**, 113102 (2003).

[16] C. R. Ast and H. Höchst, High-resolution photoemission mapping of the three-dimensional band structure of Bi (111), Phys. Rev. B **70**, 245122 (2004).

[17] P. Hofmann, The surfaces of bismuth: Structural and electronic properties, Prog. Surf. Sci. **81**, 191 (2006).

[18] L. Fu and C. L. Kane, Topological insulators with inversion symmetry, Phys. Rev. B **76**, 045302 (2007).

[19] Y. Ohtsubo, P. Le Fevre, F. Bertran, and A. Taleb-Ibrahimi, Dirac Cone with Helical Spin Polarization in Ultrathin α-Sn (001) Films, Phys. Rev. Lett. **111**, 216401 (2013).

[20] H. B. Lenoir and T. Caillat, An overview of recent developments for BiSb alloys, Semicond. Semimet. **69**, 101 (2001).

[21] P. Cucka and C. S. Barrett, The crystal structure of Bi and of solid solution of Pb, Sn, Sb and Te in Bi, Acta Crystallogr. **15**, 865 (1962).

[22] A. Tempel and B. Schumann, Determination of lattice parameters at thin epitaxial layers by RHEED, Krist. Tech. **14**, 571 (1979).

[23] Y. Ueda, N. H. D. Khang, K. Yao, and P. N. Hai, Epitaxial growth and characterization of $Bi_{1-x}Sb_x$ spin Hall thin films on GaAs(111)A substrates, Appl. Phys. Lett. **110**, 062401 (2017).

[24] L. Fu and C. L. Kane, Superconducting Proximity Effect and Majorana Fermions at the Surface of a Topological Insulator, Phys. Rev. Lett. **100**, 096407 (2008).

[25] K. Saito, H. Sawahata, T. Komine, and T. Aono, Tight-binding theory of surface spin states on bismuth thin films, Phys. Rev. B **93**, 041301(R) (2016).

[26] Y. M. Koroteev, G. Bihlmayer, E. Chulkov, and S. Blügel, First-principles investigation of structural and electronic properties of ultrathin Bi films, Phys. Rev. B **77**, 045428 (2008).

[27] Y. M. Koroteev, G. Bihlmayer, J. Gayone, E. V. Chulkov, S. Blügel, P. M. Echenique, and P. Hofmann, Strong Spin-Orbit Splitting on Bi Surfaces, Phys. Rev. Lett. **93**, 046403 (2004).

[28] T. Hirahara, T. Nagao, I. Matsuda, G. Bihlmayer, E. Chulkov, Y. M. Koroteev, P. Echenique, M. Saito, and S. Hasegawa, Role of Spin-Orbit Coupling and Hybridization Effects in the Electronic Structure of Ultrathin Bi Films, Phys. Rev. Lett. **97**, 146803 (2006).

[29] L. Petersen and P. Hedegaard, A simple tight-binding model of spin-orbit splitting of *sp*-derived surface states, Surf. Sci. **459**, 49 (2000).

[30] C. R. Ast and I. Gierz, *sp*-band tight-binding model for the Bychkov-Rashba effect in a two-dimensional electron system including nearest-neighbor contributions from an electric field, Phys. Rev. B **86**, 085105 (2012).

[31] A. Kimura, E. Krasovskii, R. Nishimura, K. Miyamoto, T. Kadono, K. Kanomaru, E. Chulkov, G. Bihlmayer, K. Shimada, and H. Namatame, Strong Rashba-Type Spin Polarization of the Photocurrent from Bulk Continuum States: Experiment and Theory for Bi (111), Phys. Rev. Lett. **105**, 076804 (2010).

[32] S. Ito, M. Arita, J. Haruyama, B. Feng, W.-C. Chen, H. Namatame, M. Taniguchi, C.-M. Cheng, G. Bian, and S.-J. Tang, Surface-state Coulomb repulsion accelerates a

metal-insulator transition in topological semimetal nanofilms, Sci. Adv. **6**, 5015 (2020).

[33] D. Kim, P. Syers, N. P. Butch, J. Paglione, and M. S. Fuhrer, Coherent topological transport on the surface of Bi_2Se_3, Nat. Commun. **4**, 2040 (2013).

[34] T. Hirahara, T. Nagao, I. Matsuda, G. Bihlmayer, E. Chulkov, Y. M. Koroteev, and S. Hasegawa, Quantum well states in ultrathin Bi films: Angle-resolved photoemission spectroscopy and first-principles calculations study, Phys. Rev. B **75**, 035422 (2007).

[35] H. Ishida, Decay length of surface-state wave function on Bi(111), J. Phys.: Condens. Matter **29**, 015002 (2016).

[36] Q. Barbedienne, J. Varignon, N. Reyren, A. Marty, C. Vergnaud, M. Jamet, C. Gomez-Carbonell, A. Lemaître, P. Le Fèvre, F. Bertran, A. Taleb-Ibrahimi, H. Jaffrès, J.-M. George, and A. Fert, Angular-resolved photoemission electron spectroscopy and transport studies of the elemental topological insulator α-Sn, Phys. Rev. B **98**, 195445 (2018).

[37] J.-C. Rojas-Sanchez, N. Reyren, P. Laczkowski, W. Savero, J.-P. Attané, C. Deranlot, M. Jamet, J.-M. George, L. Vila, and H. Jaffrès, Spin Pumping and Inverse Spin Hall Effect in Platinum: The Essential Role of Spin-Memory Loss at Metallic Interfaces, Phys. Rev. Lett. **112**, 106602 (2014).